Comparison of lower stratosphere wind observations from the USTC's Rayleigh Doppler lidar and the ESA's satellite mission Aeolus

Chong Chen[1,2], Xianghui Xue[1,2,4,5], Dongsong Sun[1,2], Ruocan Zhao[1,2], Yuli Han[1,2], Tingdi Chen[1,2], Hengjia Liu[1,2]and Yiming Zhao[6]

[1]School of Earth and Space Sciences, University of Science and Technology of China, Hefei, Anhui 230026, China
[2]Hefei National Laboratory for the Physical Sciences at the Microscale, University of Science and Technology of China, Hefei, China
[3]CAS Key Laboratory of Geospace Environment, School of Earth and Space Sciences, University of Science and Technology of China, Hefei, China
[4]CAS Center for Excellence in Comparative Planetology, Hefei, China
[5]Anhui Mengcheng Geophysics National Observation and Research Station, University of Science and Technology of China
[6]Beijing Research Institute of Telemetry, Beijing 100076, China

Key Points:

- Comparison between the USTC Rayleigh Doppler lidar winds and the Aeolus Level-2B Rayleigh winds in the stratosphere from June to December 2019.
- Overall, the Aeolus winds are consistent with the USTC lidar winds with acceptable biases.

Corresponding author: Xianghui Xue, `xuexh@ustc.edu.cn`

Abstract

Since the first space-borne Doppler wind lidar, Aeolus, was launched, global wind field observations from space have been possible. Several ground- and air-based validations followed, although most of these comparisons remained below 10 km in the troposphere, with rare validation work for the stratosphere. The Rayleigh Doppler lidar developed by the University of Science and Technology of China (USTC) was deployed in Xinjiang, China in 2017. It can observe wind speed and temperature in the stratosphere and mesosphere. By setting two geographical ranges centered on the USTC lidar, the Aeolus Rayleigh winds within these ranges can be compared with ground-based lidar wind data. Furthermore, after eliminating the effect of particulate backscatter on the USTC lidar, the lower limit of the detection range was extended to 10 km to obtain more samples. The mean biases between the Aeolus winds and the USTC lidar winds were 1.05±5.98 (-0.35±4.78) m/s, 1.80±6.30 (-1.88±4.97) m/s, and 0.17±5.45 (0.51±4.44) m/s for all data, ascending orbits, and descending orbits, respectively, in a large (small) geographical range. The results for descending orbits have a higher degree of consistency with those for ascending orbits, and the farther the distance between Aeolus observation swaths and the USTC lidar, the greater the bias. Overall, the Aeolus winds are consistent with the USTC lidar winds in the stratosphere.

1 Introduction

Given the variations in wind speed and direction, atmospheric simulation models and weather forecasting face considerable challenges(Weissmann & Cardinali, 2007; Michelson & Bao, 2008). More accurate wind field data are needed not only to advance the understanding of atmospheric processes but also to modify weather forecasting models(Stoffelen et al., 2005). Current methods used to measure wind speed and direction are mostly ground-based or airborne. Compared to these locally observing methods, global observations offer substantial advantages(Stoffelen et al., 2019; Huuskonen et al., 2014; Houchi et al., 2010; Chanin et al., 1989).

For many years, the European Space Agency (ESA) had been working on a space-borne wind lidar(ESA, 1999). In 2018, they successfully launched a low-orbit satellite, called Aeolus, for wind measurements. Similar to some ground-based lidar, the payload of this satellite, the Atmospheric Laser Doppler Instrument (ALADIN), was designed to have two different signal channels: a Fizeau interferometer to analyze the particulate backscatter narrowband signal, and another channel with a Fabry–Pérot interferometer (FPI) to obtain information regarding molecular broadband backscattered light(McKay, 2002; Gentry et al., 2000; Tepley et al., 1993). Thus, by calculating the Doppler shift of the light, the wind speed perpendicular to its orbit can be continuously retrieved(ESA, 1999; Stoffelen et al., 2005; Reitebuch, 2012; Kanitz et al., 2019). The instrument also has the capacity to acquire the distribution of the optical properties of aerosols and clouds in the direction of the line of sight(Flamant et al., 2008; Ansmann et al., 2007).

Regular calibration and validation are needed for instruments utilizing direct detection. As such, Aeolus wind data must be compared with other independent wind products(Dabas et al., 2008; Lux et al., 2018). To achieve this goal, the Aeolus team compared the wind products with extensive actual ground-based and airborne measurements(Witschas et al., 2020; Baars, Herzog, Heese, et al., 2020; Baars, Geiß, et al., 2020; Baars, Herzog, Engelmann, et al., 2020; Albertema, 2019) and atmospheric models(Rennie & Isaksen, 2020). The German Aerospace Center (Deutsches Zentrum für Luftund Raumfahrt e.V., DLR) performed two pre-launch airborne validation campaigns equipped with two lidar systems(Marksteiner et al., 2018; Lux et al., 2018; Schäfler et al., 2018). After the launch of Aeolus, Witschas et al. also conducted a validation against corresponding observations from an airborne Doppler lidar (2 μm DWL)(Witschas et al., 2020). The 2 μm DWL was used as a reference device because of its high sensitivity to particulate returns, also one of the coher-

ent detection characteristics. Rennie et al. performed the first validation of the Level-2B product by comparing it with a numerical weather prediction model. This model, developed by European Centre for Medium-Range Weather Forecasts (ECMWF), acts as a reference to generate a calibration method and assimilate the Aeolus data(Rennie & Isaksen, 2020). In addition, they found that Aeolus observations positively impact global numerical weather predictions and provide statistically significant improvements in short-range forecasts(Rennie & Isaksen, 2021). Most airborne validation campaigns were conducted over Europe, where the air is relatively clean. Over regions with severe air pollution (like some industrial cities in eastern China), however, the high levels of aerosol could decrease the accuracy of wind products. Therefore, Guo et al. investigated the quality of the wind observations of Aeolus in these regions. They compared Level-2B (L2B) winds with the winds observed by the radar wind profiler network(Guo et al., 2021), and data from 89 sites across China gave comparative results. The verifications described above were performed for portions of wind profiles at altitudes below 10 km. Baars et al. performed a unique validation by utilizing the RV *Polarstern* cruise PS116 in November/December 2018. There were six direct intersections between the concerted course and the Aeolus ground track in the Atlantic Ocean. Therefore, the six cases obtained can be compared with wind speeds at altitudes above 10 km in Aeolus, which are rare in the lower stratosphere(Baars, Herzog, Heese, et al., 2020).

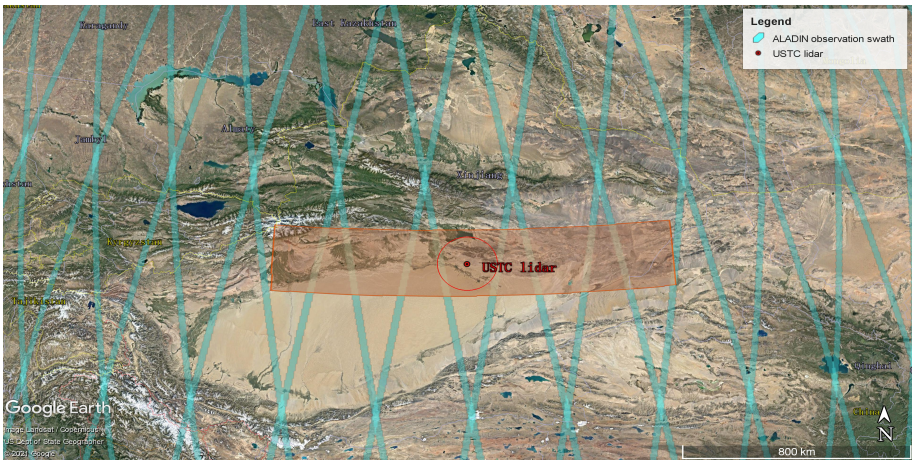

Figure 1. Location of the USTC lidar (red dot) and the ALADIN observation swath (cyan swath). The red circle is a small range for the first geographical matching principle. The red rectangle is a more extensive range for the second matching principle.

In 2018, a mobile Rayleigh Doppler lidar utilizing the double-edge technique was implemented and demonstrated by the USTC(Dou et al., 2014), capable of measuring wind and temperature in the range of 15–70 km. Zhang et al. deployed this lidar system in Xinjiang, China (41.1 °N, 87.1 °E) in 2018(Zhang et al., 2019) and validated the wind measurements by radiosonde results. The location of the lidar is shown in Fig. 1. In addition, observations with bias corrections were obtained over the period from June to December 2019.

In this paper, we assess the quality of Aeolus Rayleigh winds in the lower stratosphere by comparing them with USTC Rayleigh Doppler lidar observations from 2019. According to the distance between the ground track of Aeolus and the USTC lidar, we analyze HOLS wind profile differences in two geographic ranges. A brief introduction to the Aeolus and ground-based lidar data applied in the study is presented in Section 2. In Section 3, detailed matching principles and comparison methods are described. Sec-

tion 4 presents and discusses comparative results between Aeolus and USTC wind observations . Finally, in Section 5, we briefly conclude and outline future work.

2 Instruments and databases

2.1 Aeolus wind observations

The Aeolus satellite developed by the ESA was successfully launched in August 2018. It is a pioneering project in global wind monitoring and its payload is the direct detection DWL system, ALADIN. The satellite orbits in a sun-synchronous orbit at an altitude of 320 km, with an orbital inclination of 97° and a period of seven days. The instrument has a length of 2.9 km per horizontal measurement and takes 0.4 seconds. For the Level-2B wind products used in this study, 30 measurements are gathered together into one group whose length is defined as one observation length. In the vertical direction, the instrument provides wind profiles at the range of 0–30 km, with a resolution of 0.25 to 2 km(Stoffelen et al., 2019). The vertical resolution depends on the altitude, and the value in the stratosphere is mostly around 1 to 2 km. To classify two types of measurement bins in different air conditions, the backscatter ratio (the ratio of the sum of the scattering cross-sections of molecule and aerosol to the scattering cross-section of molecule) for each bin in the group is calculated from the raw signal data. "Cloudy" bins usually have a backscatter ratio larger than 1.2 to 1.4, according to Level-2B processor settings; nevertheless, "clear" bins have a smaller backscatter ratio than the threshold. The processor then accumulates the same type of signals horizontally in the observation group and uses different methods to retrieve various types of data separately. This method avoids systematic errors caused by contamination from particulate backscatter signals(Lux et al., 2020).

Since 12 May 2020, the Aeolus Level-2B wind product has been released to the public after some correction procedures. The product contains the horizontal line of sight (HLOS) wind velocities for the Mie and Rayleigh channels, validity flags, estimated errors, geolocations, and altitudes of the observations. It is noteworthy that the estimated error is an indispensable parameter, the theoretical value of which is determined by the signal-to-noise ratio (SNR) and the Rayleigh channel response sensitivity to atmospheric temperature and pressure(Dabas et al., 2008). The quality of one Aeolus wind could be described by the estimated error and validity flag (0 for invalid data, 1 for valid data). Considering that the valid Mie-cloudy wind observations in the stratosphere are too rare to be statistically representative, we focused on the winds of Rayleigh channel.

2.2 USTC lidar wind observations

As mentioned in the introduction, the USTC lidar has the capability to measure wind and temperature simultaneously. Some key parameters of the system are indicated in Table 1, and Fig. 2 shows the optical structure diagram of the USTC lidar. This lidar operates with an eye-safe 354.7 nm wavelength laser and adopts a 1 m diameter Cassegrain telescope with a field of view (FOV) of 0.09 mrad. The collected signal is guided to the Fabry–Pérot interferometer (FPI) by a 200 μm diameter multimode fiber (Fiber 1 in Fig. 2). Similar to ALADIN, the FPI is equipped to acquire the Doppler frequency shift of the broadband molecular (Rayleigh) backscatter signal, which can be translated into wind speed(Dabas et al., 2008; Dou et al., 2014). It is noteworthy that a weak beam of light from the laser also enters the FPI through an integrating sphere (IS) and Fiber 3 as a zero Doppler shift reference light. Thus, the drift of the retrieved wind profile can be eliminated(Zhang et al., 2019). Two subsystems with telescopes inclined at 30° are responsible for measuring the two horizontal components of wind that are perpendicular to each other. In Xinjiang, the telescope of one subsystem faces east, measuring the zonal wind, and an-

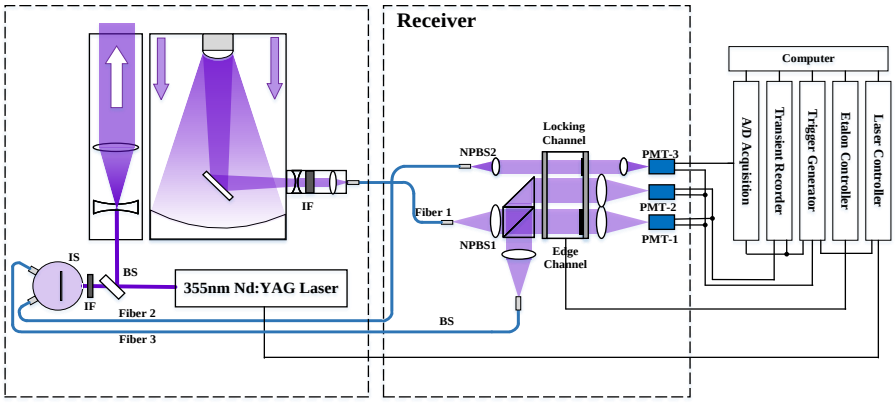

Figure 2. Schematic setup of the USTC mobile Rayleigh Doppler lidar.

other faces south, measuring the meridional wind. In addition, one subsystem with a vertical-pointing telescope measures the temperature.

Parameter	Value
Laser wavelength (nm)	354.7
Laser energy/pulse (J)	0.2
Laser repetition rate (Hz)	100
Telescope diameter (m)	1
FOV of telescope (mrad)	0.09
Zenith angle (deg)	30
Fabry–Pérot Etalon FSR (GHz)	12.5
Peak transmission (%)	60
PMTs Quantum Efficiency (%)	21

Table 1. Key parameters of the USTC lidar system.

During the six-month observation period from June 2019, on clear nights, the instrument was in operation from 8:00 p.m. to 6:00 a.m. (local time is six hours ahead of the universal time) in summer, and 6:00 p.m. to 6:00 a.m. in winter when the nighttime is longer. To eliminate the adverse effects of contamination from particulate backscatter signals, the measurement range was set to 15–70 km, where the air is relatively clean. However, we reset the lower altitude limit to 10 km to increase the number of wind samples for comparison. Systematic errors due to particulate backscatter signals in the range of 10–15 km are discussed below. More detailed descriptions of the calibration of the USTC lidar system can be found in Zhang's study(Zhang et al., 2019). The vertical height and temporal resolution of the wind data used in this study are 200 m and 30 min. We select HLOS wind data with an SNR greater than 42.5 (corresponding to an error of 4 m/s), which results in smaller error than the estimated error of Aeolus winds for most of the horizontal synthetic winds.

3 Method

Since the temporal and spatial resolutions of Aeolus and USTC lidar data are different—i.e., the Aeolus wind profile has a vertical resolution of 250–2000 m, mostly 1–2 km in the stratosphere, whereas the USTC lidar wind profile has a vertical resolution of 200 m–a reasonable matching process is needed to make the comparison. Fig. 3 shows a flowchart of pre-processing for the USTC and the Aeolus winds.

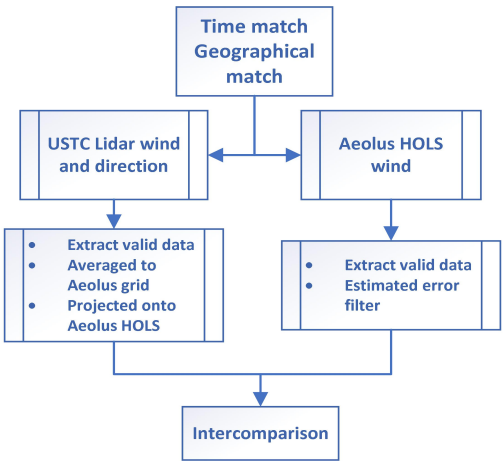

Figure 3. Flowchart of the pre-processing procedures for comparing USTC lidar winds with Aeolus winds.

The wind is relatively stable in the stratosphere at a mid-latitude region in China(Dou et al., 2014; Shu et al., 2012). Therefore, the USTC lidar wind measurement time must be within six hours before and after and closest to the Aeolus observation time. Meanwhile, two different geographical matching principles are presented in Fig. 1. Considering the USTC lidar was located in the middle of two Aeolus observation swaths, the distance between the USTC lidar and Aeolus observation swath should be less than 85 km. The red circle in Fig. 1 shows the range of the first matching principle. It covers observation swaths (indicated by cyan swaths) for one ascending orbit and one descending orbit. The Aeolus observations in the red circle are close enough to the USTC lidar. However, samples for comparison are too rare to sufficiently validate the quality of Aeolus wind data. We applied another geographical matching principle based on a more extensive range that covers observation swaths for four ascending orbits and five descending orbits. The red rectangular in Fig. 1 represents this new range, where the lidar position coordinates are ± 7 degrees of longitude and ± 1 degree of latitude. The samples in this range are selected as a supplement for comparison. If more than one Aeolus wind profile satisfies the matching principle for the USTC lidar wind profile, only one profile with the shortest horizontal distance will be selected.

In the next step, we filtered the data, as mentioned above, to obtain valid USTC wind data. The highest and lowest points of the USTC lidar wind profiles were then matched with the Aeolus data to select the wind profiles with overlapping ranges. The USTC lidar data always completely covered the content of the Aeolus wind profile in the field of comparison, i.e., 10–30 km, and the vertical resolution of the lidar data was higher. Therefore, we used linear interpolation to interpolate the USTC lidar wind data by the height corresponding to the Aeolus wind profile. Then, the USTC lidar wind vector averaged into every Aeolus vertical bin was projected onto the HLOS direction of Aeolus wind as follows(Witschas et al., 2020):

$$v_{lidar_{HLOS}} = \cos(\Psi_{Aeolus} - wd_{lidar}) \cdot ws_{lidar}, \tag{1}$$

where Ψ_{Aeolus} is the wind azimuth angle acquired from the Aeolus L2B product, and ws_{lidar} and wd_{lidar} represent the velocity and direction of USTC lidar wind, respectively.

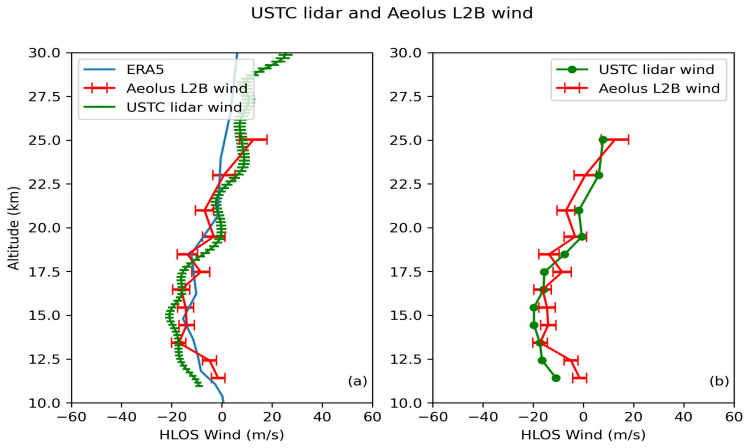

Figure 4. Example lidar wind profile into HLOS and interpolated into Aeolus grids. (a) The projected USTC lidar wind is indicated by the green line with error bars. The Aeolus L2B Rayleigh HLOS wind and its estimated error are indicated by the red line with error bars. The blue line represents the ERA5 data (also projected into HLOS). (b) The USTC lidar HLOS wind is interpolated into the Aeolus height grids. The lines represent the same as those in (a).

An example is given in Fig. 4. The wind velocity profile was obtained by USTC lidar at 10:30 (UTC), and the Aeolus wind profile was measured at 6:20 (UTC) on September 19, 2019. The central location of the Aeolus measurements is at 40.7 °N, 88.0 °E, which is very close to the USTC lidar. The latest climate reanalysis produced by ECMWF, the ERA5 horizontal wind profile(B, 2018), is also shown in Fig. 4. Considering the temporal and spatial resolution of the ERA5 data, we chose the closest wind profile: 40.75 °N, 88.00 °E at 6:00 (UTC). Overall, the two wind profiles observed by USTC lidar and Aeolus, as well as the ERA5 wind profile, have the same trend with height. The ERA5 wind and the Aeolus wind are smaller than the USTC lidar wind below 12.5 km, whereas the USTC lidar profile is in better agreement with the Aeolus measurements above 17.5 km.

To assess the performance of the Aeolus Rayleigh HLOS winds ($v_{Aeolus_{HLOS}}$) in the stratosphere, the biases of the corresponding HLOS USTC lidar winds and the Aeolus HLOS winds ($v_{lidar_{HLOS}}$) are given by

$$v_{diff} = v_{Aeolus_{HLOS}} - v_{lidar_{HLOS}} \tag{2}$$

In good weather conditions, the UTSC lidar measurement range can be improved up to a much higher altitude than the range we discuss in this study. In Fig. 4, it can be easily noticed that the USTC lidar wind error is much smaller than the Aeolus wind error at 10–30 km. Therefore, the error of Aeolus wind is the main factor affecting the reliability of the comparison. Referring to Witchas et al. and Guo et al.(Witschas et al., 2020; Guo et al., 2021), we filtered the data to remove Aeolus Rayleigh wind with a more significant estimated error before the statistics. As shown in Fig. 5, a threshold of 7 ms^{-1} for the Aeolus estimated error kept the wind difference between the USTC lidar winds and Aeolus Rayleigh winds relatively constant and densely distributed around zero, except for in several samples. The wind differences increase significantly for those data with estimated errors larger than 7 ms^{-1}. Thus, the estimated error threshold for Rayleigh winds was set to 7 ms^{-s}.

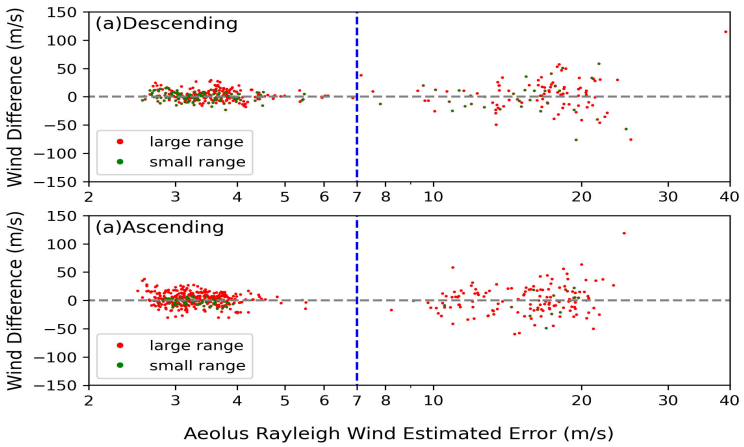

Figure 5. Biases of Aeolus HLOS winds and USTC lidar winds derived from Eq. 2 against the corresponding estimated errors given by the Aeolus L2B product. The red (green) dots represent data in a large (small) geographical range for descending orbits (a) and ascending orbits (b). The blue dashed line indicate the error threshold in this study.

Several statistical parameters give a reliable indication of the performance of Aeolus winds. The wind mean bias ($Mean_b$) and standard deviation of bias (Std_b) are given by

$$Mean_b = \frac{1}{n}\sum_{i=1}^{n} v_{diff} \tag{3}$$

and

$$Std_b = \sqrt{\frac{1}{n-1}\sum_{i=1}^{n}(v_{diff} - Mean_b)^2} \tag{4}$$

where n is the number of valid data pairs. Besides the two parameters above, the correlation coefficient (R) between the USTC lidar and Aeolus winds is calculated.

4 Comparison results

4.1 Results

Through the method described above, from June to September 2019, we obtained 647 samples in a large geographical range (LGR) and 173 samples in a small geographical range (SGR), covering altitudes from 10–30 km for comparison (shown in Fig. 6). Since the USTC lidar typically has a detection range of more than 15 km, we discuss the data point pairs in the altitude ranges of 10–15 km and more than 15 km separately. For wind data pairs below 15 km, the values of R are 0.58 (descending) and 0.55 (ascending) in the LGR, 0.68 (descending), and 0.63 (ascending) in SGR. The values of R in the SGR are slightly larger than those in the LGR, which may result from wind varying significantly along the horizontal distance at the lower stratosphere. Except for the linear fit result for ascending orbits in the LGR (the slope is 0.81), the slopes are far from 1 (0.56 for descending orbits in the LGR, 0.58 for descending orbits in the SGR, and 0.41 for ascending orbits in the SGR). Thus, the biases of the USTC lidar winds and Aeolus winds are relatively large in both geo-ranges. This result is expected at the lower stratosphere, where the wind speeds vary more dramatically with horizontal distance and time than at higher altitudes.

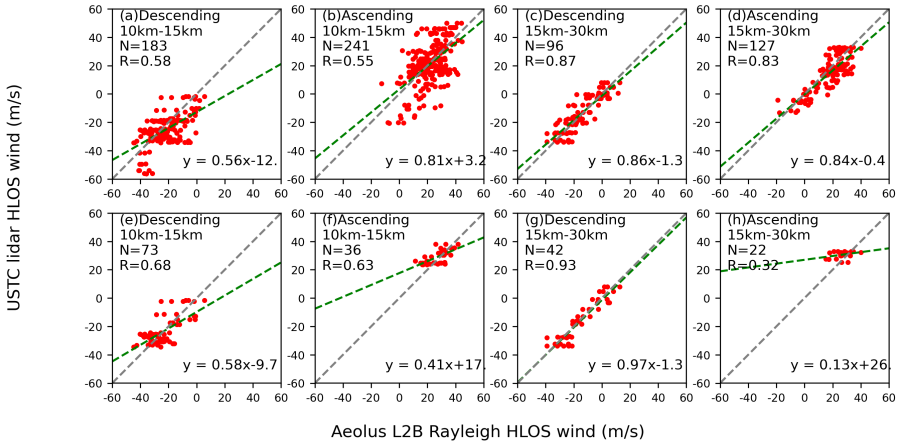

Figure 6. Aeolus against the USTC lidar Rayleigh HLOS winds for (a, b, c, and d) larger geographical range and (e, f, g, and h) smaller geographical range, for (a, b, e, and f) winds in the range of 10–15 km and (c, d, g, and h) winds in range above 15 km, for (a, c, e, and g) descending orbits and (b, d, f, and h) ascending orbits. The corresponding least squared linear fit results are shown by green dashed lines. The fit results, number of data point pairs N, and correlation coefficients R are also shown in the insets, and $y = x$ is indicated by gray dashed lines.

For data pairs above 15 km, there are fewer samples than below 15 km. The values of R are 0.87 (0.93) for descending orbits in the LGR (SGR), and 0.83 (0.32) for ascending orbits in the LGR (SGR). The slopes of linear fit are 0.86 (0.97) for descending orbits in the LGR (SGR), and 0.84 (0.13) for ascending orbits in the LGR (SGR). With the exception of the data pairs for ascending orbits in the SGR, all the other Aeolus winds are consistent with the USTC lidar winds at this height. The USTC lidar winds, as well as Aeolus winds for ascending orbits in the SGR, vary between small cells around 30 m/s, and the number of samples is only 22, which is too small. Therefore, the results of the linear fit and correlation coefficient are not enough to reflect the true bias of the two winds. Fig. 7 indicates the vertical distribution of the mean bias between the Aeolus HLOS winds and the USTC lidar winds in the LGR. In the range where the number of samples is more than 3, the maximum mean bias for descending (ascending) orbits is 6.65 (6.94) m/s. The standard deviation of bias values increases with decreasing altitude, with a maximum value of 13.32 (14.44) m/s for descending (ascending) orbits. The standard deviation of the biases remains within a relatively low level above 15 km, with a maximum value of 7.56 (8.88) m/s for descending (ascending) orbits.

A similar situation exists for the SGR (shown in Fig. 8). The mean and standard deviation of the biases at lower altitudes are larger than those at higher altitudes, indicating that the biases have a remarkable dependency on the altitude. The mean biases for descending orbits are all negative, for both the LGR and SGR below 12.5 km, because the velocity of the USTC lidar winds is larger than Aeolus winds at this height. As mentioned above, the normal observation range of the USTC lidar is above 15 km. Hence, the contamination of particulate backscatter can be ignored. To further investigate the performance of Aeolus products at the bottom of the stratosphere, it is essential to assess the influence of particulate backscatter signals received by the USTC lidar below 15 km.

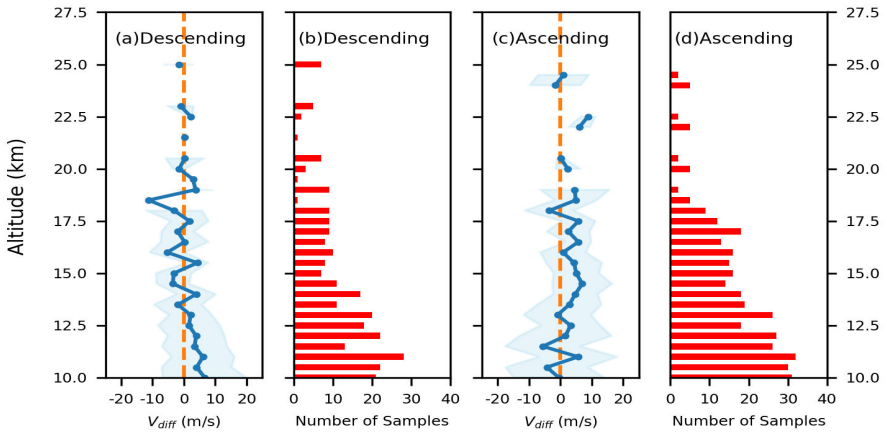

Figure 7. Vertical distribution of the mean biases between the Aeolus HLOS winds and the USTC lidar HLOS winds and number of samples for (a and b) descending orbits and (c and d) ascending orbits in a large geo-range. The blue lines represent the mean biases, and the blue shadowed areas represent the standard deviation. The horizontal red bars represent the number of samples at each height. The orange dashed lines represent zero biases.

4.2 Influence of particulate backscattering

According to the way lidar works, the retrieved wind speed at altitudes below 15 km is biased, as there is no energy monitor channel for numerical iterations to remove the aerosol contribution(Dou et al., 2014). An approximate algorithm proposed by Klett and Fernald is thus applied to retrieve the lidar backscatter ratio(Fernald, 1984). An example is provided in Fig. 9(a), showing that the USTC lidar HLOS wind profile is consistent with the Aeolus HLOS wind profile above 13 km. However, the bias of the two winds increases rapidly below 12.5 km, the same altitude where the backscatter ratio grows beyond 1.2. Strong particulate backscatter signals may lead to deviations in the Rayleigh scattering spectrum, and may even cause the saturation of PMTs, resulting in significant systematic errors. In the next step, the retrieved winds within the height range where the backscatter ratio is greater than 1.2 (the shadowed area in Fig. 9(a)) are removed. A scatter plot of the Aeolus winds against the USTC lidar winds after the process is presented in Fig. 9(b). It can be seen that the scatter distribution is in a smaller range around the mean value compared with that in Fig. 6. The mean biases between the two winds is 1.80±6.30 (-1.88±4.97) m/s, 0.17±5.45 (0.51±4.44) m/s, and 1.05±5.98 (-0.35±4.78) m/s for ascending orbits, descending orbits, and all data in the LGR (SGR), respectively. The details of the linear fit and statistical parameters are tabulated in Table 2. The slopes of linear fits are 0.94 (0.52), 0.78 (0.94), and 0.88 (1.02) for all data, ascending orbits, and descending orbits in the LGR (SGR), respectively. The values of R are 0.96 (0.35), 0.84 (0.95), and 0.89 (1.02) for all data, ascending orbits, and descending orbits in the LGR (SGR), respectively. Overall, most results are more expected, except that the slope and R of data pairs for ascending orbits in the SGR are distorted due to the small sample size.

After eliminating the effect of the particulate backscatter signal, we found that the Aeolus Rayleigh winds agree well with the USTC lidar winds from the stratosphere. Moreover, the results for descending orbits have a higher degree of consistency than those for ascending orbits. Fig. 10 shows the vertical distribution of the mean biases with a backscatter ratio filter. The number of samples below 15 km drops by around half compared to before filtering, and the maximum of mean biases (standard deviations of bias) are re-

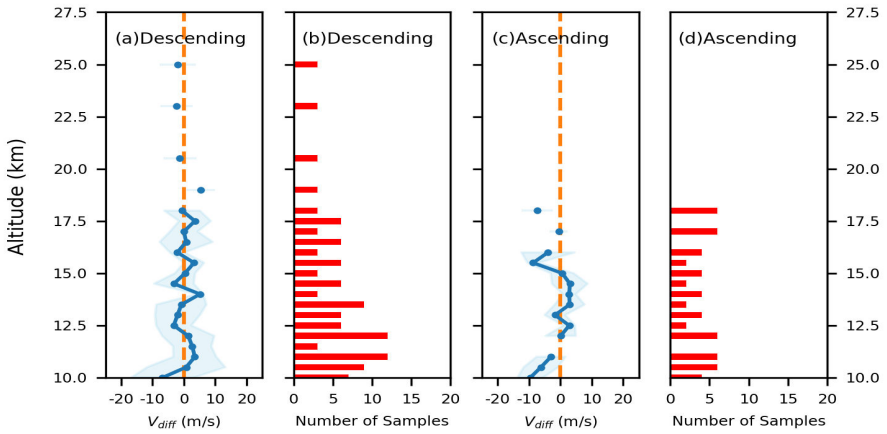

Figure 8. Vertical distribution of the mean biases between the Aeolus HLOS winds and the USTC lidar HLOS winds and number of samples for (a and b) descending orbits and (c and d) ascending orbits in a small geo-range. The lines, shadows, and the histograms represent the same as those in Fig. 7.

	Ascending		Descending		All	
	LGR	SGR	LGR	SGR	LGR	SGR
Number	204	43	173	76	377	119
Mean (m/s)	1.80	-1.88	0.17	0.51	1.05	-0.35
Std (m/s)	6.30	4.97	5.45	4.44	5.98	4.78
R	0.84	0.52	0.89	0.94	0.96	0.98
Slope	0.78	0.35	0.88	0.95	0.94	1.02
Intercept	5.77	20.57	-1.89	-1.52	-0.89	0.40

Table 2. Statistical comparison of Aeolus HLOS winds and USTC lidar winds.

duced to 4.17 (8.69) m/s and 3.14 (8.06) m/s for ascending orbits and descending orbits, respectively. The results barely change above 15 km, where the atmosphere is relatively clean.

4.3 Geographical distance from the observation swaths

Another relevant factor risks skewing the results, namely, the horizontal distance between the Aeolus observation swaths and the USTC lidar. We derived the results under the assumption that the variation of wind speeds is insignificant in a limited region with the same latitude. However, a brief discussion of the influence of geographic distance is needed. Fig. 11 shows the mean bias and number of samples for each orbit at different longitudes. The numbers of samples of Aeolus winds are 15 and 11 for descending orbits at 81.6 °E and ascending orbits at 82.8 °E, respectively. As such, the number of samples is insufficient for a statistically valid comparison. The mean biases of the remaining three ascending orbits at 85.6 °E, 88.8 °E, and 91.9 °E are -1.93±4.49 m/s, 2.39±5.34 m/s, and 6.23±7.24 m/s, respectively. The results for descending orbits at 88.2 °E and 91.5 °E are 0.39±4.61 m/s and -1.40±5.65 m/s, respectively. Overall, the farther the distance between the Aeolus observation swath and the USTC lidar, the greater the bias, indicating that the horizontal distance slightly influences the comparison re-

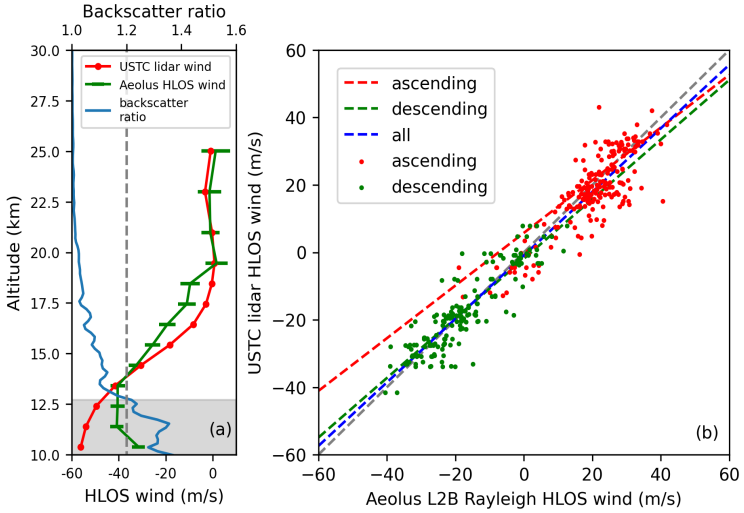

Figure 9. (a) Interpolated USTC lidar HLOS wind profile (red line) and Aeolus HLOS wind profile (green line with error bars) at 6:06 a.m., Aug. 28, 2019 (UTC), and the vertical distribution of the backscatter ratio (blue line). The shadowed area covers the height range with a backscatter ratio greater than 1.2. (b) Aeolus against the USTC lidar HLOS winds filtered for the backscatter ratio for ascending orbits (red dots) and descending orbits (green dots). The linear fit results are given for ascending orbits (red dotted line), descending orbits (green dotted line), and all data (blue dotted line). The gray dotted line indicates $y = x$.

sults. The Aeolus winds for ascending orbits at 88.8 °E and 91.9 °E, and for descending orbits at 88.2 °E, would be more suitable for a comparison with the USTC lidar winds. Likewise, it is evident that the wind products for descending orbits are better than those for ascending orbits. The Aeolus winds correspond to different orbits, implying different measurement times(Stoffelen et al., 2005), i.e., in the morning for descending orbits and in the evening for ascending orbits. This demonstrates that the accuracy of Aeolus Rayleigh winds is also influenced by the time of observation.

5 Conclusion

This paper showed the results of the USTC Rayleigh Doppler lidar winds compared to the Aeolus L2B Rayleigh winds in the stratosphere from June to December 2019. The lower limit of the vertical detection range of the USTC lidar was extended to 10 km, thus increasing the number of data pairs available for comparison. Data from two geographically different sizes were discussed separately to assess the performance of Aeolus winds in this study. After eliminating the effect of particulate backscatter signals using the Klett–Fernald algorithm, the mean biases were calculated at 1.05±5.98 m/s in LGR and -0.35±4.78 in SGR, indicating that the Aeolus winds are consistent with the USTC lidar winds. It is expected that the farther the horizontal distance between the USTC lidar and Aeolus observation swaths, the greater the bias. For the three most suitable orbits for comparison, the mean biases were -1.93±4.49 m/s and 2.39±5.34 m/s for ascending orbits at 85.6 °E and 88.8 °E, respectively, and 0.39±4.61 m/s for descending orbits at 88.2 °E. This may be an effect of the different times of observation. The effect of seasonal variation on the results was not discussed in this paper, as the sample size varies too much from season to season to be statistically representative. However, further work can be carried out when more ground-based lidar winds and Aeolus winds are obtained.

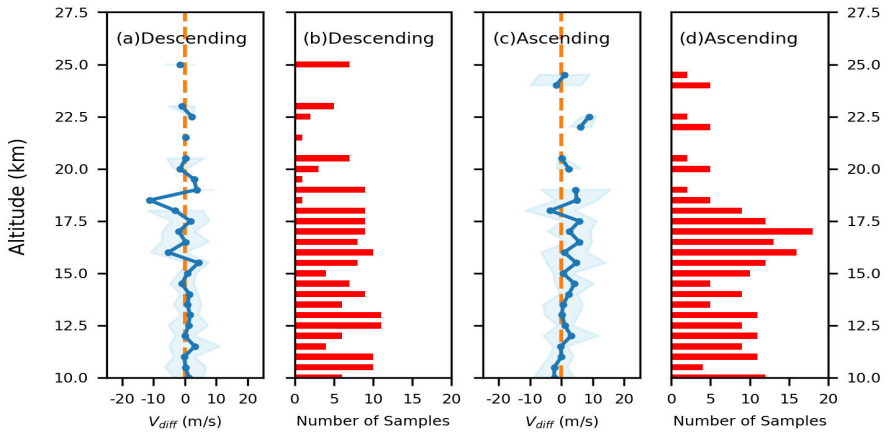

Figure 10. Vertical distribution of the mean biases between the Aeolus HLOS winds and the USTC lidar winds filtered for the backscatter ratio, and the number of samples for descending orbits (a and b) and ascending orbits (c and d). The lines, shadows, and histograms represent the same as those in Fig. 7.

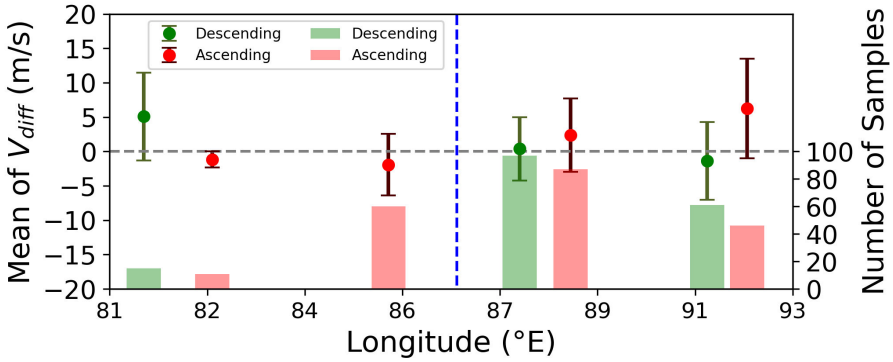

Figure 11. Mean bias between Aeolus HLOS winds and the USTC lidar winds, and the number of samples for each orbit at different longitudes. The winds are filtered for the backscatter ratio. The red (green) dots show the mean bias with error bars, representing the corresponding standard deviation for ascending (descending) orbits. The histograms indicate the number of samples. The blue dotted line shows the longitude of the USTC lidar.

Acknowledgments

We thank Prof. Xianghui Xue and Prof. Dongsong Sun for their valuable suggestions regarding the observation results. We acknowledge data resources from the National Space Science Data Center, National Science and Technology Infrastructure of China (`https://www.nssdc.ac.cn`) and the Ground-based Space Environment Network. We are grateful to the European Center for Medium-range Weather Forecasts for providing the ERA5 data. This work is supported by National Natural Science Foundation of China (Grant Nos. 41904136, 41774193, and 42104146), Key-Area Research and Development Program of Guangdong Province (2020B0303020001), Shanghai Municipal Science and Technology Major Project (Grant No. 2019SHZDZX01), and the Fundamental Research Funds for the Central Universities.

The USTC lidar wind profiler data presented in this paper are not publicly available but may be obtained from the authors upon reasonable request. The Aeolus wind products can be downloaded from `https://aeolus-ds.eo.esa.int/oads/access/collection`. The ERA5 data can be downloaded from `https://cds.climate.copernicus.eu/`.

References

Albertema, S. (2019). *Validation of aeolus satellite wind observations with aircraft-derived wind data and the ecmwf nwp model for an enhanced understanding of atmospheric dynamics* (Unpublished master's thesis).

Ansmann, A., Wandinger, U., Le Rille, O., Lajas, D., & Straume, A. G. (2007). Particle backscatter and extinction profiling with the spaceborne high-spectral-resolution doppler lidar aladin: methodology and simulations. *Applied optics*, *46*(26), 6606–6622.

B, J. O. A. (2018). Era5: The new champion of wind power modelling? *Renewable Energy*, *126*, 322-331.

Baars, H., Geiß, A., Wandinger, U., Herzog, A., Engelmann, R., Bühl, J., ... others (2020). First results from the german cal/val activities for aeolus. In *Epj web of conferences* (Vol. 237, p. 01008).

Baars, H., Herzog, A., Engelmann, R., Bühl, J., Radenz, M., Seifert, P., ... others (2020). Validation of aeolus aerosol and wind products with sophisticated ground-based instruments in the northern and southern hemisphere. In *Egu general assembly conference abstracts* (p. 14242).

Baars, H., Herzog, A., Heese, B., Ohneiser, K., Hanbuch, K., Hofer, J., ... Wandinger, U. (2020). Validation of aeolus wind products above the atlantic ocean. *Atmospheric Measurement Techniques*, *13*(11), 6007–6024.

Chanin, M.-L., Garnier, A., Hauchecorne, A., & Porteneuve, J. (1989). A doppler lidar for measuring winds in the middle atmosphere. *Geophysical research letters*, *16*(11), 1273–1276.

Dabas, A., Denneulin, M., Flamant, P., Loth, C., Garnier, A., & Dolfi-Bouteyre, A. (2008). Correcting winds measured with a rayleigh doppler lidar from pressure and temperature effects. *Tellus A: Dynamic Meteorology and Oceanography*, *60*(2), 206–215.

Dou, X., Han, Y., Sun, D., Xia, H., Shu, Z., Zhao, R., ... Guo, J. (2014). Mobile rayleigh doppler lidar for wind and temperature measurements in the stratosphere and lower mesosphere. *Optics express*, *22*(105), A1203–A1221.

ESA. (1999). The four candidate earth explorer core missions—atmospheric dynamics mission. *ESA Report for Mission Selection ESA SP-*, *1233*(4), 145–pp.

Fernald, F. G. (1984). Analysis of atmospheric lidar observations: some comments. *Applied optics*, *23*(5), 652–653.

Flamant, P., Cuesta, J., Denneulin, M.-L., Dabas, A., & Huber, D. (2008). Adm-aeolus retrieval algorithms for aerosol and cloud products. *Tellus A: Dynamic Meteorology and Oceanography*, *60*(2), 273–286.

Gentry, B. M., Chen, H., & Li, S. X. (2000). Wind measurements with 355-nm molecular doppler lidar. *Optics letters*, *25*(17), 1231–1233.

Guo, J., Liu, B., Gong, W., Shi, L., Zhang, Y., Ma, Y., ... others (2021). First comparison of wind observations from esa's satellite mission aeolus and ground-based radar wind profiler network of china. *Atmospheric Chemistry and Physics*, *21*(4), 2945–2958.

Houchi, K., Stoffelen, A., Marseille, G., & De Kloe, J. (2010). Comparison of wind and wind shear climatologies derived from high-resolution radiosondes and the ecmwf model. *Journal of Geophysical Research: Atmospheres*, *115*(D22).

Huuskonen, A., Saltikoff, E., & Holleman, I. (2014). The operational weather radar network in europe. *Bulletin of the American Meteorological Society*, *95*(6), 897–907.

Kanitz, T., Lochard, J., Marshall, J., McGoldrick, P., Lecrenier, O., Bravetti, P., ... Elfving, A. (2019). Aeolus first light: first glimpse. In *International conference on space optics—icso 2018* (Vol. 11180, p. 111801R).

Lux, O., Lemmerz, C., Weiler, F., Marksteiner, U., Witschas, B., Rahm, S., ... Reitebuch, O. (2018). Airborne wind lidar observations over the north atlantic in 2016 for the pre-launch validation of the satellite mission aeolus. *Atmospheric Measurement Techniques*, *11*(6), 3297–3322.

Lux, O., Lemmerz, C., Weiler, F., Marksteiner, U., Witschas, B., Rahm, S., ... Reitebuch, O. (2020). Intercomparison of wind observations from the european space agency's aeolus satellite mission and the aladin airborne demonstrator. *Atmospheric Measurement Techniques*, *13*(4), 2075–2097.

Marksteiner, U., Lemmerz, C., Lux, O., Rahm, S., Schäfler, A., Witschas, B., & Reitebuch, O. (2018). Calibrations and wind observations of an airborne direct-detection wind lidar supporting esa's aeolus mission. *Remote Sensing*, *10*(12), 2056.

McKay, J. A. (2002). Assessment of a multibeam fizeau wedge interferometer for doppler wind lidar. *Applied optics*, *41*(9), 1760–1767.

Michelson, S. A., & Bao, J.-W. (2008). Sensitivity of low-level winds simulated by the wrf model in california's central valley to uncertainties in the large-scale forcing and soil initialization. *Journal of Applied Meteorology and Climatology*, *47*(12), 3131–3149.

Reitebuch, O. (2012). The spaceborne wind lidar mission adm-aeolus. In *Atmospheric physics* (pp. 815–827). Springer.

Rennie, M. P., & Isaksen, L. (2020). An assessment of the impact of aeolus doppler wind lidar observations for use in numerical weather prediction at ecmwf. In *Egu general assembly conference abstracts* (p. 5340).

Rennie, M. P., & Isaksen, L. (2021). An update on the impact of aeolus doppler wind lidar observations for use in numerical weather prediction at ecmwf. In *Egu general assembly conference abstracts* (pp. EGU21–1254).

Schäfler, A., Craig, G., Wernli, H., Arbogast, P., Doyle, J. D., McTaggart-Cowan, R., ... others (2018). The north atlantic waveguide and downstream impact experiment. *Bulletin of the American Meteorological Society*, *99*(8), 1607–1637.

Shu, Z.-f., Dou, X.-k., Xia, H.-y., Sun, D.-s., Han, Y., Cha, H.-K., ... Hu, D.-d. (2012). Low stratospheric wind measurement using mobile rayleigh doppler wind lidar. *Journal of the Optical Society of Korea*, *16*(2), 141–144.

Stoffelen, A., Kumar, R., Zou, J., Karaev, V., Chang, P. S., & Rodriguez, E. (2019). Ocean surface vector wind observations. In *Remote sensing of the asian seas* (pp. 429–447). Springer.

Stoffelen, A., Pailleux, J., Källén, E., Vaughan, J. M., Isaksen, L., Flamant, P., ... others (2005). The atmospheric dynamics mission for global wind field measurement. *Bulletin of the American Meteorological Society*, *86*(1), 73–88.

Tepley, C. A., Sargoytchev, S. I., & Rojas, R. (1993). The doppler rayleigh lidar system at arecibo. *IEEE transactions on geoscience and remote sensing*, *31*(1), 36–47.

Weissmann, M., & Cardinali, C. (2007). Impact of airborne doppler lidar observations on ecmwf forecasts. *Quarterly Journal of the Royal Meteorological Society: A journal of the atmospheric sciences, applied meteorology and physical oceanography*, *133*(622), 107–116.

Witschas, B., Lemmerz, C., Geiß, A., Lux, O., Marksteiner, U., Rahm, S., ... Weiler, F. (2020). First validation of aeolus wind observations by airborne doppler wind lidar measurements. *Atmospheric Measurement Techniques*, *13*(5), 2381–2396.

Zhang, N., Sun, D., Han, Y., Chen, C., Wang, Y., Zheng, J., ... Tang, L. (2019). Zero doppler correction for fabry–pérot interferometer-based direct-detection

doppler wind lidar. *Optical Engineering*, *58*(5), 054101.